In Proceedings "3D Image Analysis and Synthesis '97", November 17-18, 1997, Erlangen, Germany,
edited by H.-P. Seidel, B. Girod, H. Niemann, pp. 115-122, Sankt Augustin: infix
doi: 10.5281/zenodo.16452

Multichannel Shape from Shading Techniques for Reconstruction of Specular Surfaces

Günther Balschbach[2], Jochen Klinke[3], and Bernd Jähne[1,2,3]

[1]Interdisciplinary Center for Scientific Computing
[2]Institute for Environmental Physics
University of Heidelberg, Im Neuenheimer Feld 368, D-69120 Heidelberg, Germany
[3]Physical Oceanography Research Division
Scripps Institution of Oceanography, University of California, La Jolla, CA 92093-0230, USA
Bernd.Jaehne@iwr.uni-heidelberg.de, gbalsch@dali.uphys.uni-heidelberg.de, jklinke@ucsd.edu

Abstract

This paper describes a shape from shading technique for the reconstruction of specular surfaces based on refraction and color illumination or multiple pulsed light sources. The technique is used to retrieve the small-scale shape of wave-undulated water surfaces in the laboratory and the field.

1 Introduction

Shape form shading is one of the basic paradigms in computer vision for 3-D reconstruction [*Horn*, 1977]. This technique is based on the elementary interaction of surfaces with illumination. The object radiance that is perceived from an observer generally depends on the direction of the surface normal with respect to the incident rays from illumination sources and the ray reflected in the direction of the camera.

Unfortunately shape from shading techniques with a single illumination of the scene are nonlinear, ambiguous, and are rather a qualitative than a quantitative technique for surface reconstruction. Deviations from the assumed bidirectional reflectance function cause significant systematic errors. Furthermore, standard shape from shading techniques cannot handle specular reflectance.

In environmental sciences, the surface of oceans, lakes, and rivers constitutes a surface with *specular* reflectance characteristics. Recently, the fine-scale structure of this surface in the millimeter to meter range undulated by wind- or flow-generated waves has received increasing interest for two reasons.

Figure 1: SAR image of the Dutch coast including the islands Fleeland and Terschelling taken with the SEASAT satellite. In the open ocean, ship tracks can be observed, while in the mud-flats between the islands strong variations in the radar backscatter can be observed caused by strong tidal currents that are modulated by the varying water depth. Image courtesy of Dr. E. van Halsema, TNO, the Netherlands.

First, modern active remote sensing techniques based on microwaves (radar scatterometry) "sees" these small structures [*Apel*, 1987]. By various interactions between the small-scale features and larger-scale features the latter become visible in synthetic aperture radar (SAR) images [*Komen and Oost*, 1989]. As an example, Fig. 1 shows a SAR image of the Dutch coast in which ship tracks and tidal currents are visible.

Second, short wind waves significantly influence the exchange processes between the atmosphere and the oceans. The regular wave motion may become unstable and break even on small scales without air entrainment and thus en-

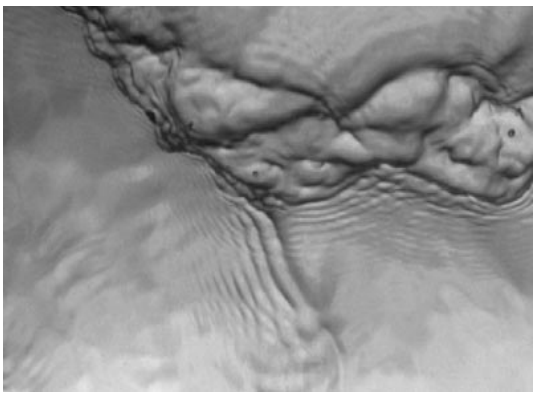

Figure 2: A microscale wave breaking event at 5 m/s wind speed as observed with the instrument shown in Fig. 15. The image sector is about $15 \times 20\,\mathrm{cm}^2$. From *Klinke and Jähne* [1995].

hances the exchange, for instance, of climate relevant gases such as CO_2 significantly [*Liss and Duce*, 1997; *Jähne and Haußecker*, 1998]. Such an event, known as microscale wave breaking, is shown in Fig. 2.

Thus there is a considerable interest to measure the small-scale shape of this dynamical interface. For almost a century, oceanographers tried to use optical techniques — mostly stereo photography — but without much success [*Jähne et al.*, 1994]. Only with the advent of modern computer vision technology, it became feasible to solve this demanding measuring problem. Because of the dynamical nature of the surface, techniques that retrieve the shape from a series of consecutive images are not suitable.

This paper first reviews as an introduction the classical shape from shading technique based on reflectance from a Lambertian surface in Sect. 2. Then it is discussed how multiple illuminations can be used to determine surface gradients without ambiguity (Sect. 3). Refraction-based techniques for transparent and dynamic specular surfaces are introduced in Sects. 4 and 5 and some results are discussed in Sect. 6.

2 Shape from Shading for Lambertian Surfaces

For the sake of simplicity, we assume that the surface of a Lambertian object is illuminated by parallel light. Then, the radiance of the surface,

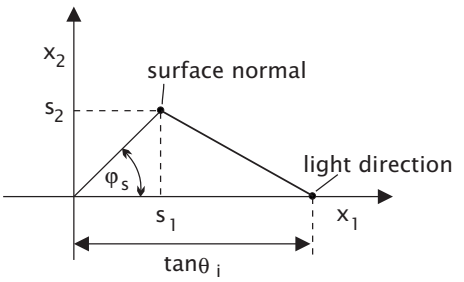

Figure 3: Radiance computation illustrated in the gradient space for a Lambertian surface illuminated by a distant light source with an incidence angle θ_i and an azimuthal angle ϕ_i of zero.

L, is given by:

$$L = \frac{\rho(\lambda)}{\pi} E \cos\gamma, \tag{1}$$

where E is the irradiance and γ the angle between the surface normal and the light direction. The relation between the surface normal and the incident and exitant radiation can most easily be understood in the *gradient space*. This space is spanned by the gradient of the surface height $a(X, Y)$:

$$\boldsymbol{s} = \nabla a = \left[\frac{\partial a}{\partial X}, \frac{\partial a}{\partial Y} \right] = \left[s_1, s_2 \right]. \tag{2}$$

This gradient is directly related to the surface normal $\boldsymbol{n}$ by

$$\boldsymbol{n} = \left[-\frac{\partial a}{\partial X}, -\frac{\partial a}{\partial Y}, 1 \right]. \tag{3}$$

This equations says that the gradient space can be understood as a plane parallel to the XY plane at a height $Z = 1$ if we invert the directions of the X and Y axes. The X and Y coordinates where the surface normal vector and other directional vectors intersect this plane are the corresponding coordinates in the gradient space.

The geometry of Lambertian reflection in the gradient space is illustrated in Fig. 3. Without loss of generality, we set the direction of the light source as the x direction. Then, the light direction is given by the vector $\boldsymbol{l} = (\tan\theta_i, 0, 1)^T$, and the radiance L of the surface can be expressed as

$$\begin{aligned} L &= \frac{\rho(\lambda)}{\pi} E \frac{\boldsymbol{s}^T \boldsymbol{l}}{|\boldsymbol{s}||\boldsymbol{l}|} \\ &= \frac{\rho(\lambda)}{\pi} E \frac{s_1 \tan\theta_i + 1}{\sqrt{1 + \tan^2\theta_i}\sqrt{1 + s_1^2 + s_2^2}}. \end{aligned} \tag{4}$$

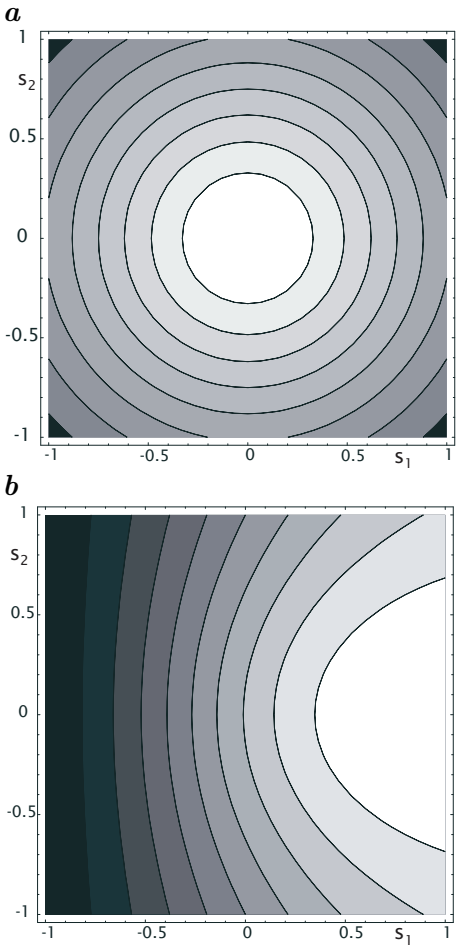

Figure 4: Contour plot of the radiance of a Lambertian surface with homogeneous reflectivity illuminated by parallel light shown in the gradient space for surface slopes between -1 and 1. The radiance is normalized to the radiance for a flat surface. **a** Zero incidence angle $\theta_i = 0$; the spacing of the contour lines is 0.05. **b** Oblique illumination with an incidence angle of 45° and an azimuthal angle of 0°; the spacing of the contour lines is 0.1.

Contour plots of the radiance distribution in the gradient space are shown in Fig. 4a for a light source with an incidence angle of $\theta_I = 0$. In the case of the light source at the zenith, the contour lines of equal radiance mark lines with constant absolute slope $s = (s_1^2 + s_2^2)^{1/2}$. However, the radiance changes with surface slope are low, especially for low surface inclinations. An oblique illumination leads to a much higher contrast in the radiance (Fig. 4b). With an oblique illumination, however, the maximum surface slope in the direction opposite to the light source is limited to

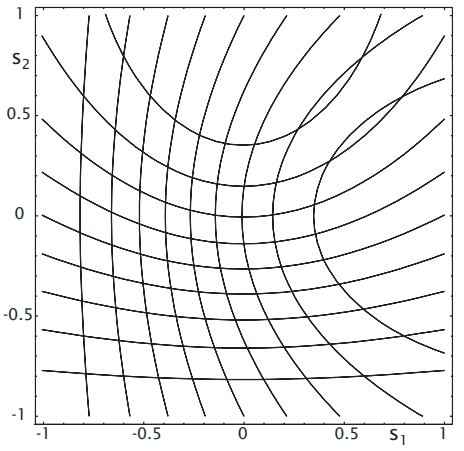

Figure 5: Superimposed contour plots of the radiance of a Lambertian surface with homogeneous reflectivity illuminated by a light source with an angle of incidence of 45° and an azimuth angle of 0° and 90°, respectively.

$\pi/2 - \theta$ when the surface normal is perpendicular to the light direction.

The curved contour lines indicate that the relation between surface slope and radiance is nonlinear. This means that even if we take two different illuminations of the same surface (Fig. 5), the surface slope may not be determined in a unique way. This is the case when the curved contour lines intersect each other at two points.

3 Multi-Illumination Shape from Shading

Using three exposures has the advantage that the surface gradient can be retrieved unambigiously and that the inhomogeneities in the surface reflectivity or in the illumination cancel out. As an example system, we illuminate a Lambertian surface with the same light source from the following three different directions:

$$\begin{aligned} \boldsymbol{l}_1 &= (0, 0, 1) \\ \boldsymbol{l}_2 &= (\tan\theta_i, 0, 1) \\ \boldsymbol{l}_3 &= (0, \tan\theta_i, 1). \end{aligned} \tag{5}$$

Then

$$L_{2,3}/L_1 = \frac{s_{1,2}\tan\theta_i + 1}{\sqrt{1 + \tan^2\theta_i}}. \tag{6}$$

Now the equations are linear in s_1 and s_2 and — even better — they are decoupled: s_1 and s_2 depend only on L_2/L_1 and L_3/L_1, respectively (Fig. 6). In addition, the normalized radiance in

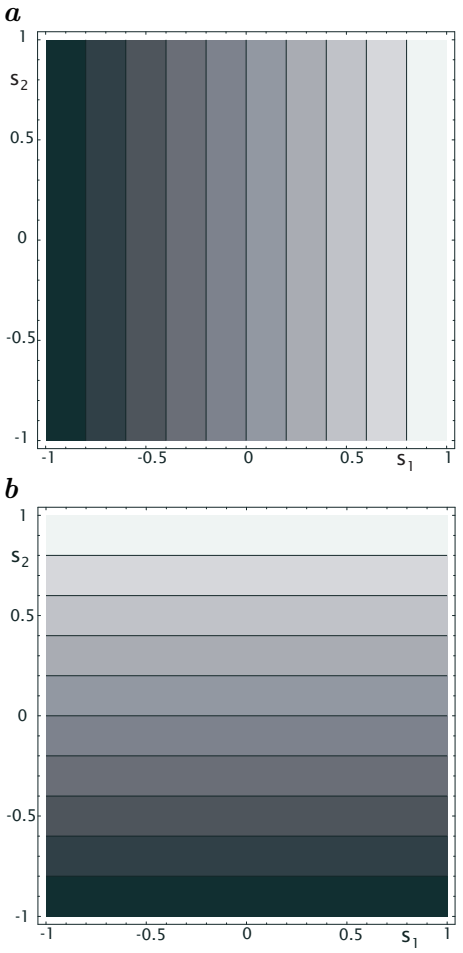

Figure 6: Contour plots of the radiance of a Lambertian surface illuminated by parallel light with an incidence angle of 45° and an azimuth angle of 0° (**a**) and 90° (**b**), respectively, and normalized by the radiance of the illumination at 0° incidence according to (6). The step size of the contour lines is 0.1.

(6) does not depend on the reflectivity of the surface. The reflectivity of the surface is contained in (1) as a factor and thus cancels out when the ratio of two radiance distributions of the same surface is computed.

4 Shape from Refraction for Specular Surfaces

For specular surfaces, the shape from shading techniques discussed in Sects. 2 and 3 do not work at all since light is only reflected towards the camera, when the angle of incidence from the light source is equal to the angle of reflectance. Thus, extended light sources are required. A detailed analysis [*Jähne et al.*, 1994]

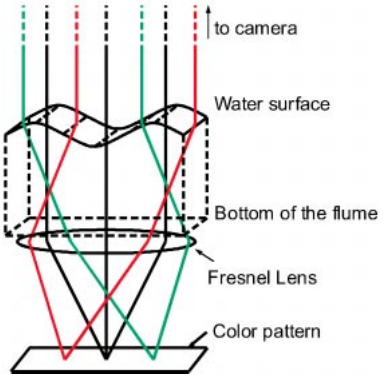

Figure 7: Telecentric illumination system for shape from refraction: an extended light source is located in the focal plane of a fresnel lens.

showed that for transparent specular surfaces, *shape from refraction* techniques are more advantageous than shape from reflection techniques because the radiance is higher, steeper surface slopes can be measured, and the nonlinearities in the slope/radiance relationship are significantly lower.

The base of the shape from refraction technique is a *telecentric illumination system* which converts a spatial radiance distribution into an angular radiance distribution (Fig. 7). Then, all we have to do is to compute the relation between the surface slope and the angle of the refracted beam and to use a light source with an appropriate spatial radiance distribution.

Figure 8 illustrates the optical geometry for the simple case when the camera is placed far above and a light source below a transparent surface of a medium with a higher index of refraction. The relation between the surface slope s and the angle γ is given by *Jähne et al.* [1994] as

$$\begin{aligned} s &= \tan\alpha = \frac{n\tan\gamma}{n-\sqrt{1+\tan^2\gamma}} \\ &\approx 4\tan\gamma\left[1+\frac{3}{2}\tan^2\gamma\right] \end{aligned} \tag{7}$$

with $n = n_2/n_1$. The inverse relation is

$$\begin{aligned} \tan\gamma &= s\frac{\sqrt{n^2+(n^2-1)s^2}-1}{\sqrt{n^2+(n^2-1)s^2}+s^2} \\ &\approx \frac{1}{4}s\left(1+\frac{3}{32}s^2\right). \end{aligned} \tag{8}$$

In principle, the shape from refraction technique works for slopes up to infinity (vertical surfaces). In this limiting case, the ray to the camera

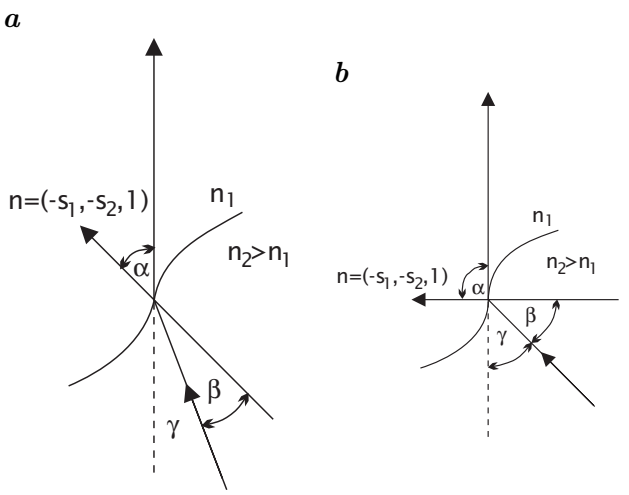

Figure 8: Refraction at an inclined surface as the base for the shape from refraction technique. The camera is far above the surface. **a** Rays emitted by the light source at an angle γ are refracted in the direction of the camera. **b** Even for a slope of infinity (vertical surface, $\alpha = 90\,°$), rays from the light source meet the camera.

grazes the surface (Fig. 8b) and

$$\tan\gamma = \sqrt{n^2 - 1}. \tag{9}$$

The refraction law thus causes light rays to be inclined in a certain direction relative to the slope of the water surface. If we make the radiance of the light source dependent on the direction of the light beams, the water surface slope becomes visible. The details of the construction of such a system is described by *Jähne et al.* [1994]. Here we just assume that the radiance of the light rays is proportional to the $\tan\gamma$ in x_1 direction. Then we obtain the relation

$$L \propto s_1 \frac{\sqrt{n^2 + (n^2-1)s^2} - 1}{\sqrt{n^2 + (n^2-1)s^2 + s^2}}. \tag{10}$$

Of course, we have again the problem that from a scalar quantity such as the radiance no vector component such as the slope can be inferred. The shape from refraction technique, however, comes very close to an ideal setup. If the radiance varies only linearly in the x_1 direction, as assumed, the radiance map in the gradient space is also almost linear (Fig. 9). A slight influence of the cross slope (resulting from the nonlinear terms in (10) in s^2) becomes apparent only at quite high slopes.

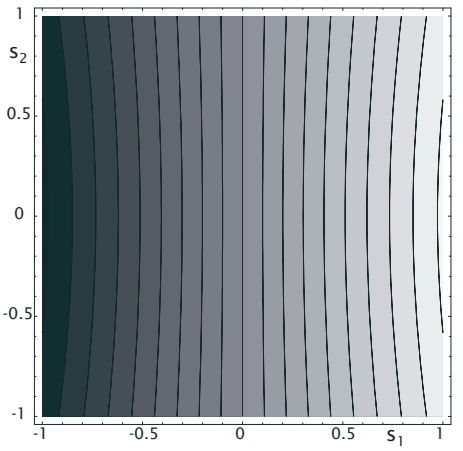

Figure 9: Radiance map for the shape from refraction technique where the radiance in a telecentric illumination source varies linearly in the x_1 direction.

5 Multi-Illumination Shape from Refraction

The shape form refraction technique described in the previous section with a single illumination source has been used extensively to compute wave number spectra from wave slope images [*Jähne and Riemer*, 1990] and is described in detail by *Jähne et al.* [1994]. New in this paper is the use of multiple illuminations simultaneously. *Zhang and Cox* [1994] were the first to describe a surface gradient instrument based on color imaging utilizing the HSI color space. Here we describe a simpler and more accurate approach based on linear illumination gradients in the RGB color space.

Color images have three independent primary colors: red, green, and blue. With a total of three channels, we can identify the position in an illumination system — and thus the inclination of the water surface — uniquely and still have one degree of freedom left for corrections (Fig. 7). With color imaging we also have the advantage that all three illuminations are taken simultaneously. Thus moving objects can also be observed.

A unique position coding with color can be achieved, for example, with the following additive color wedges (Fig. 10):

$$\begin{aligned} G(\boldsymbol{s}) &= (1/2 + cx_1)E_0(\boldsymbol{s}) \\ R(\boldsymbol{s}) &= [1/2 - c/2(x_1 + x_2)]E_0(\boldsymbol{s}) \\ B(\boldsymbol{s}) &= [1/2 - c/2(x_1 - x_2)]E_0(\boldsymbol{s}). \end{aligned} \tag{11}$$

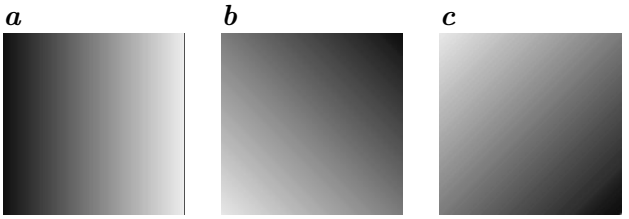

Figure 10: Radiance of the extended light source for the shape from refraction instrument shown in Fig. 7: **a** green, **b** red, and **c** blue channel.

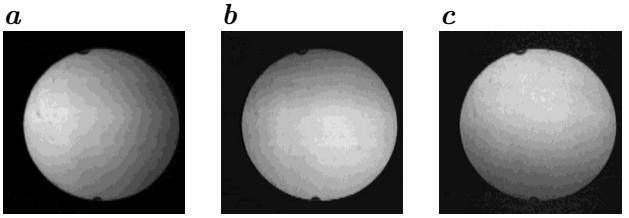

Figure 11: Green (**a**), red **b**), and blue **c**) component of an RGB color image taken from a calibration target, a spherical lens.

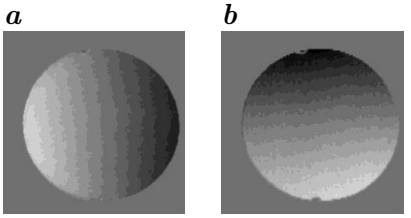

Figure 12: Images showing the slope of a spherical lens in **a** x and **b** y direction retrieved from the images in Fig. 11.

We have again assumed a linear relation between one component of the slope and the radiance, with nonlinear isotropic corrections of the form $s_1 E_0(\boldsymbol{s})$; c is a calibration factor relating the measured radiance to the surface slope.

We now have three illuminations to determine two slope components. Thus, we can take one to compensate for unwanted spatial variation of E_0. This can be done by normalizing the three color channels by the sum of all channels $G+R+B$:

$$\begin{aligned} \frac{G}{G+R+B} &= \frac{2}{3}\left(\frac{1}{2}+cx_1\right), \\ \frac{B-R}{G+R+B} &= \frac{2}{3}cx_2. \end{aligned} \tag{12}$$

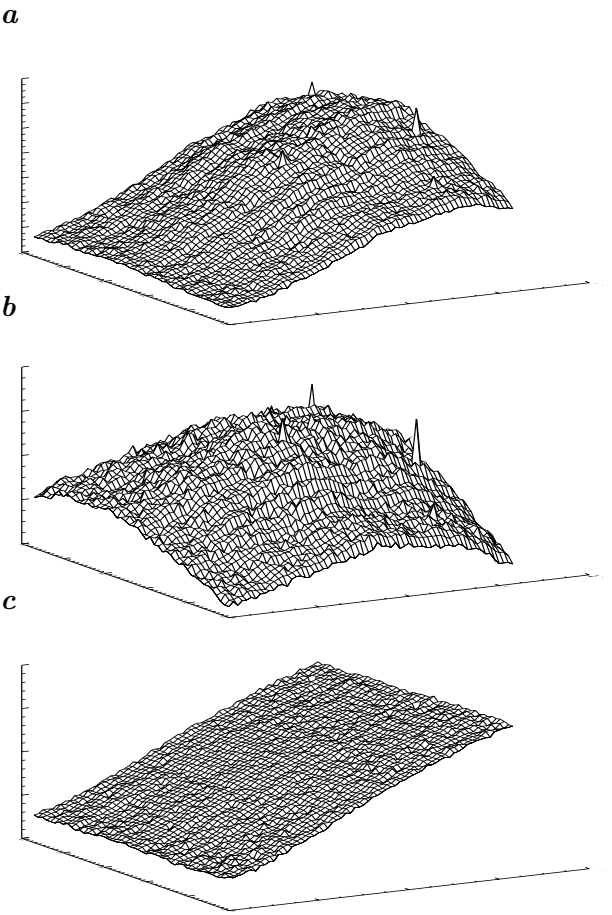

Figure 13: Demonstration of the suppression of inhomogeneities in the luminance by the color shape from refraction technique. **a** original green component of the intensity wedge, **b** luminance of **a**, **c** normalized green component

Then the position on the wedge from which the light originates is given as

$$\begin{aligned} x_1 &= \frac{3}{2c}\left(\frac{G}{G+R+B}-\frac{1}{3}\right), \\ x_2 &= \frac{3}{2c}\frac{B-R}{G+R+B}. \end{aligned} \tag{13}$$

From these position values, the x and y components of the slope can be computed using $\tan\gamma_{1,2} = x_{1,2}/f$ and (7).

An alternative to color imaging is a setup with multiple light sources of the same color. Separation between the different illuminations is then achieved by pulsing the light sources shortly after each other. Shuttered cameras are synchronized in such a way that one camera sees only one light pulse. In this way, a quasi-simultaneous measurement with different illumination becomes possible. Such a system was used on a freely drifting

buoy (Fig. 15) for ocean measurements to avoid errors caused by wavelength-dependent absorption and scattering in sea water.

6 Results

One of the calibration techniques uses a spherical lens. Since this object shows a constant curvature, the slope components in x and y directions vary linearly in the corresponding directions. The original green, red, and blue images show considerable intensity decreases towards the edge of the calibration object (Fig. 11). In the slope images, normalized using (13), this intensity drop is compensated.

The suppression of illumination inhomogeneities is nicely demonstrated in Fig. 13. This time, the color illumination source is directly observed through a flat water surface by removing the lens of the illumination system (Fig. 7). Bubbles and dirt on the glass window at the bottom of the water channel lead to considerable small-scale spatial intensity fluctuations in the green channel (Fig. 13a). Furthermore, the intensity drop towards the edge of the illumination source makes the spatial intensity variation nonlinear and leads at the right edge even into an inversion of the direction of the spatial intensity gradient. The normalization technique according to (13) suppresses both errors and results in a linear intensity variation (Fig. 13c).

Figure 14 demonstrates the technique with real wave images taken in the circular wind/wave facility of Heidelberg University. The original images (Fig. 14a, c, e) show significant intensity variations caused by the array of fluorescent lamps. In the images showing the along-wind and cross-wind wave slope components (Fig. 14d, f), these intensity variations are almost entirely suppressed. Figure 14b shows a height reconstruction with a simple Fourier transform technique using the slope images Fig. 14d, f.

7 Conclusions

The multiple-illumination shape from refraction techniques proved to be a useful technique to reconstruct the shape of dynamically changing, transparent and specular reflecting surfaces, such as water surfaces. Further work will concentrate on a careful error analysis, further improvement of the accuracy, measurements of very steep slopes, and field measurements with freely drifting buoys (Fig. 15).

Acknowledgments

Financial support for this research by the German Science Foundation (Deutsche Forschungsgemeinschaft, DFG) through the Forschergruppe "Bildfolgenanalyse zum Studium dynamischer Prozesse" (Jae 395/6-1) is gratefully acknowledged. Cooperation with Scripps Institution of Oceanography (SIO) and the field experiments were made possible by grants of the US National Science Foundation (Coastal Ocean Processes, CoOP) and the US Office of Naval Research (ONR) through the Marine Boundary Layer Accelerated Research Initiative (MBL/ARI).

References

[1] J. R. Apel. *Principles of Ocean Physics*, Academic Press, London, 1987.

[2] B. K. P. Horn. Understanding image intensities, *Artificial Intelligence*, 8:201–231, 1977.

[3] B. Jähne and H. Haußecker. Air-Water Gas Exchange, *Annual Review of Fluid Mechanics*, 30, 1998 (in press).

[4] B. Jähne, J. Klinke, and S. Waas. Imaging of short ocean wind waves: a critical theoretical review. *J. Optical Soc. Amer. A*, 11:2197–2209, 1994.

[5] B. Jähne and K. Riemer. Two-dimensional wave number spectra of small-scale water surface waves, *J. Geophys. Res.*, 95:11,531–11,546, 1990.

[6] J. Klinke and B. Jähne. Measurement of short ocean wind waves during the MBL-ARI west coast experiment. In B. Jähne and E. Monahan, editors, *Air-Water Gas Transfer, Selected Papers, 3rd Intern. Symp. on Air-Water Gas Transfer*, pages 165–173, Aeon, Hanau, 1995.

[7] G. Komen and W. Oost, (eds.). *Radar scattering from modulated wind waves.* Dordrecht: Reidel, 1989.

[8] P. S. Liss and R. A. Duce (eds.). *The sea surface and global change*, Cambridge Univ. Press, Cambridge, UK, 1997.

[9] X. Zhang and C. S. Cox. Measuring the two dimensional structure of a wavy water surface optically: a surface gradient detector. *Exp. Fluids*, 17:225, 1994.

Preprint, Tagungsband Herbsttagung des Graduiertenkollegs "3D Bildanalyse und -synthese", 17.–18. November 1997, H.-P. Seidel, B. Girod, H. Niemann (Hrsg.), Universität Erlangen Nürnberg

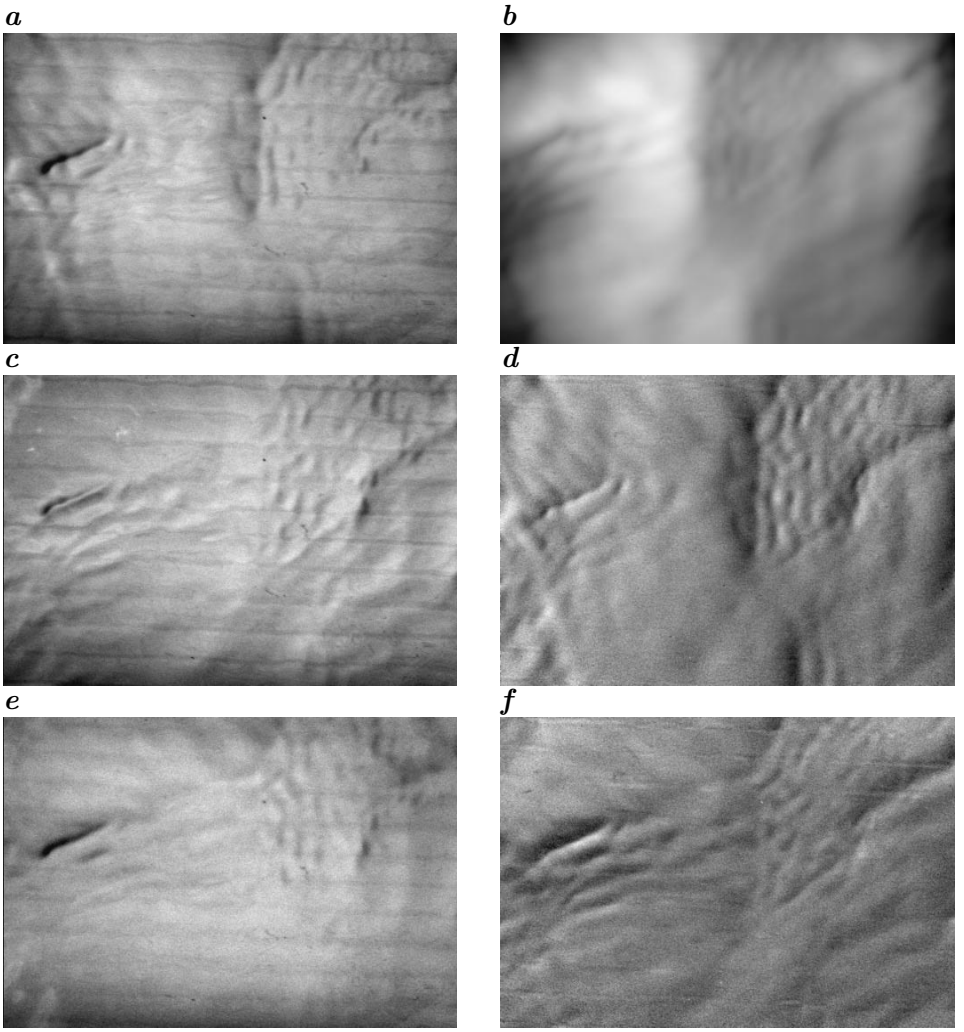

Figure 14: **a**, **c**, and **e**, green, red, and blue component of the original color image, respectively. **b** Reconstructed height; **d** and **f** images of the slope in x and y direction, respectievly.

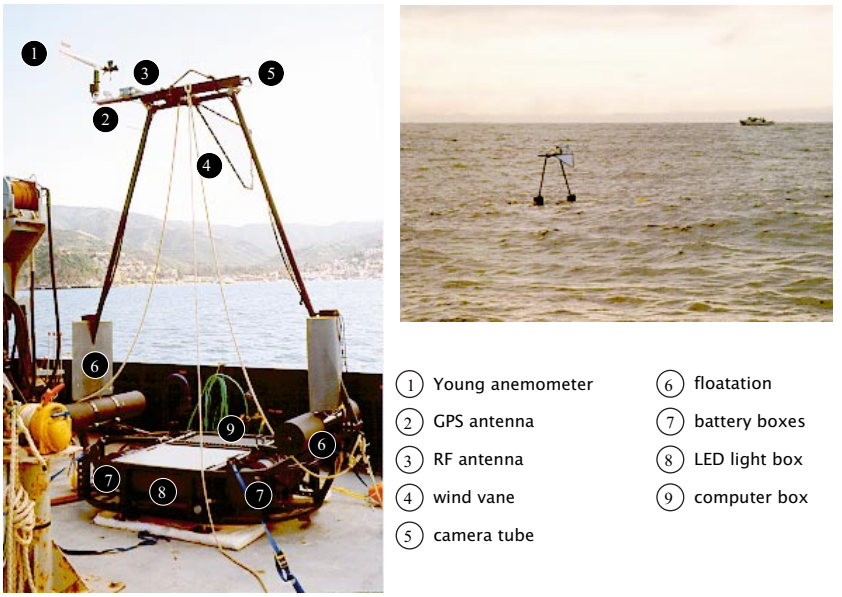

Figure 15: Buoy for imaging of short wind waves using the shape from refraction technique.